

¹ **Global changes in oceanic mesoscale currents over the satellite altimetry record**

³ Josué Martínez-Moreno¹, Andrew McC. Hogg¹, Matthew H. England², Navid C. Constantinou¹,
⁴ Andrew E. Kiss¹ & Adele K. Morrison¹

⁵ ¹*Research School of Earth Sciences and ARC Centre of Excellence for Climate Extremes, Aus-*
⁶ *tralian National University, Canberra, ACT, Australia*

⁷ ²*Climate Change Research Centre and ARC Centre of Excellence for Climate Extremes, Univer-*
⁸ *sity of New South Wales, Sydney, NSW, Australia*

⁹ **Oceanic mesoscale eddies play a profound role in mixing tracers such as heat, carbon, and**
¹⁰ **nutrients, thereby regulating regional and global climate. Yet, it remains unclear how the**
¹¹ **eddy field has varied over the past few decades. Furthermore, climate model predictions**
¹² **generally do not resolve mesoscale eddies, which could limit their accuracy in simulating fu-**
¹³ **ture climate change. Here we show a global statistically significant increase of ocean eddy**
¹⁴ **activity using two independent observational datasets of surface mesoscale eddy variability,**
¹⁵ **one estimates surface currents and the other is derived from sea surface temperature. Maps**
¹⁶ **of mesoscale variability trends show heterogeneous patterns, with eddy-rich regions showing**
¹⁷ **a significant increase of 2% - 5% per decade, while the tropical oceans show a decrease in**
¹⁸ **mesoscale variability. This readjustment of the surface mesoscale ocean circulation has im-**
¹⁹ **portant implications for the exchange of heat and carbon between the ocean and atmosphere.**

²⁰ Changes in the climate system over recent decades have warmed the upper ocean and modi-

21 fied the wind stress, heat and freshwater fluxes that drive ocean circulation^{?,?}. These changes have
22 the capacity to modify the ocean circulation, including the overturning circulation^{?,?}, basin-scale
23 gyres^{?,?} and boundary currents^{?,?}. Changes in climate can also affect mesoscale processes, for
24 example through changes in wind stress forcing over the Southern Ocean[?]. The oceanic mesoscale
25 incorporates motions that occur at spatial scales from approximately 10 to 100 km. These motions
26 include both steady flows (e.g. jets and recirculations) and time-varying flows (e.g. meanders
27 and coherent vortices). Generally, time-varying mesoscale flows are also referred to as eddies.
28 Mesoscale eddies are ubiquitous in the global ocean and feed back onto all scales, from regional
29 processes[?] up to the global meridional overturning circulation[?]. Moreover, these eddies act to
30 transport and mix tracers such as heat, salt, and nutrients^{?,?}. Thus, understanding the evolution of
31 the mesoscale circulation is crucial to formulating better predictions of our changing oceans.

32 Kinetic energy (KE) quantifies the magnitude of ocean currents^{?,?,?,?}. Kinetic energy is
33 proportional to the square of the velocity, and is commonly separated into the mean KE (MKE;
34 computed from the time-mean velocity field) and the KE of the time-varying velocity (known as
35 the eddy kinetic energy; EKE). The EKE is dominated by mesoscale variability and is a significant
36 fraction of the total KE^{?,?}. A recent study has inferred a global increase of KE anomaly from ocean
37 reanalyses and Argo floats[?]. However, these reanalyses and observations do not have the spatial
38 resolution required to resolve the mesoscale field. Moreover, the ECCO ocean state-estimate shows
39 a slight speed up of the currents, with a weak trend of surface kinetic energy[?]. In contrast, satellite
40 observations resolve the mesoscale field at latitudes between 60°S - 60°N, and suggest that EKE
41 in the Southern Ocean and Northeastern Pacific have a robust increasing trend^{?,?,?,?}. However, the

42 global multi-decadal trends of mesoscale eddy activity from satellite observations are yet to be
43 quantified.

44 Mesoscale flows have a footprint in both sea surface height (SSH) and sea surface temper-
45 ature (SST). EKE can be directly inferred from SSH via geostrophy, and mesoscale eddies act
46 to strain and shear the temperature field, meaning that regions of high EKE are associated with
47 strong mesoscale SST gradients. Therefore, observed SST gradients can be considered a proxy of
48 mesoscale eddies^{?, ?, ?}.

49 In this study we examine the evolution of mesoscale eddies using satellite observations of
50 SSH and SST over the satellite altimetry record (1993 - 2020). We use two independent datasets,
51 namely AVISO+ SSH and NOAA optimum interpolated sea surface temperature (OISST v2.1)[?],
52 to estimate EKE and SST gradients respectively (see Methods). These fields are then temporally
53 smoothed using a running average of 12 months to eliminate the seasonal cycle. The trends and
54 the significance of each field are computed using a linear regression and a modified Mann–Kendall
55 test[?] (see Methods for further details). Mesoscale variability is spatially heterogeneous; thus we
56 explore the trends of mesoscale eddies both globally and regionally.

57 Global mesoscale eddy trends

58 Over the last three decades, ocean thermal expansion and melting of land ice have led to an
59 increase of SSH^{?, ?} (Fig. 1a). This SSH increase can be observed in all ocean basins, but there
60 is also regional variability (Fig. 1b). SSH gradients are proportional to the surface geostrophic
61 flow, from which we can compute velocity anomalies and eddy kinetic energy (see Methods). The

62 time-mean EKE highlights eddy-rich regions including boundary currents and their extensions, the
63 Antarctic Circumpolar Current (ACC), and the equatorial band (Fig. 1d). These oceanic eddy-rich
64 regions show statistically significant trends over the satellite altimetry record 1993-2020 (Fig. 1f),
65 which suggest a regional long-term adjustment of the ocean mesoscale eddy field. Moreover, the
66 global surface area-integrated EKE has a positive trend of $\sim 1.2\%$ per decade ($0.09 \pm 0.04 \text{ PJ m}^{-1}$
67 decade $^{-1}$; Fig. 4c; statistically significant at the 95% confidence level). The spatial structure of
68 EKE trends is highly heterogeneous, although its zonal average shows significant net tendencies,
69 with increasing trends observed polewards of 25°S and 40°N (Fig. 1e,f). A strengthening of the
70 EKE field is a direct indication of an increase in mesoscale currents.

71 Sea surface temperature is an independent dataset relative to SSH, but is also influenced by
72 mesoscale eddies and has better temporal and spatial resolution than SSH. SST has increased
73 on multi-decadal timescales due to climate change^{?,?} (Fig. 2a), with a heterogeneous global spa-
74 tial pattern modulated by interdecadal climate variability[?] (Fig. 2b). The time-mean SST gradi-
75 ents again highlight eddy-rich regions, such as boundary currents, their extensions, and the ACC
76 (Fig. 2d). These regions with large SST gradients also exhibit some of the largest positive SST
77 gradient trends, while the subtropical gyres and the tropics mostly exhibit a decreasing trend
78 (Fig. 2e,f). The global area-integrated SST gradient magnitude has increased at a rate of $3.9 \pm$
79 $1.33 \times 10^6 \text{ }^\circ\text{C m decade}^{-1}$ (Fig. 4e) or 0.2% per decade (95% confidence level) relative to the
80 global time-mean area-integrated SST gradient magnitude ($1.7 \times 10^9 \text{ }^\circ\text{C m}$). Moreover, SST gra-
81 dients are enhanced by stretching and straining due to mesoscale eddies. Further analysis shows
82 that mesoscale SST gradients (Extended Data Fig. 3; length-scales smaller than 3°; see Methods)

83 dominate the observed trends, increasing at a rate of $5.37 \pm 0.94 \times 10^6 \text{ } ^\circ\text{C m decade}^{-1}$ (0.4% per
84 decade; statistically significant at the 95% confidence level). This analysis confirms that the ob-
85 served SST gradient trends are a consequence of the mesoscale eddy field stirring the temperature
86 field.

87 Eddy kinetic energy and mesoscale SST gradients show analogous spatial and temporal re-
88 sponses in the boundary currents and their extensions, the ACC and the tropics. Note that eddy-rich
89 regions such as the Kuroshio Current, the Agulhas retroflection, the Gulf Stream, and the East Aus-
90 tralian Current show large changes in mesoscale SST gradients co-located with some of the largest
91 EKE changes (Fig. 3). Even though these fields do not match perfectly, we quantified the areas of
92 same-sign trend for each of these four regions (Extended Data Fig. 4). We find that the increasing
93 and decreasing trends of SST and EKE match to a good extent for the Kuroshio Current, the Agul-
94 has retroflection, and the East Australian Current (61% - 65% of same-sign area agreement). The
95 spatial patterns of these independent satellite products further suggest an intrinsic response of the
96 mesoscale eddy field to a changing and variable climate.

97 **Spatial patterns of ocean mesoscale trends**

98 Eddy kinetic energy and mesoscale SST gradient trends both indicate a net strengthening of
99 the global mesoscale activity. However, both datasets reveal heterogeneous patterns of increas-
100 ing and decreasing trends. Thus, to further understand the spatial variability, we first focus our
101 analysis on individual area-integrated regions: namely, the Southern Ocean (by which we mean
102 south of 35°S), and the Pacific, Indian, and Atlantic Oceans north of 35°S (Fig. 4d). This analysis

reveals that the Southern Ocean and the Pacific Ocean are, to a large extent, responsible for the global area-integrated trends and variations of EKE and mesoscale SST gradients; the trends in the Indian and Atlantic Oceans are in contrast much smaller (Fig. 4a,b). The Southern Ocean shows a statistically significant increase for both the EKE and SST gradient, where the observed changes have been attributed to the strengthening of the wind stress since the early 1990s⁷. The Pacific Ocean SST gradient decreases significantly, with the EKE signal also decreasing; albeit below the 95% significance level (Fig. 4c,e). The large uncertainty in the Pacific EKE trend (orange error bars in Fig. 4c) is a consequence of the pulses in the time series during 1997 and 2015, both being El Niño onset years. These large anomalous interannual signals dominate the uncertainty of the global EKE trend.

El Niño events are associated with a strengthening of the North Equatorial Countercurrent and the northern branch of the South Equatorial Current; particularly during extreme eastern Pacific El Niños, such as those which occurred during 1997-1998 and 2015-2016⁷ (gray bars in Fig. 4a,b). During such El Niño events, the equatorial currents generate significant transient circulation anomalies that extend over the equatorial band (9°N - 9°S). After a scale decomposition of the velocities, we observe that these EKE pulses correspond to features located within the equatorial band and have scales larger than the typical mesoscale eddy size⁷ (approximately 10 to 100 km; see Methods; Extended Data Fig. 5a,c). Thus, equatorial currents during El Niño events modulate the equatorial EKE response and the strong interannual variability conceals EKE trends over the equatorial region.

123 To further investigate the effect of El Niño events on the mesoscale, we remove the equato-
124 rial regions (9°S – 9°N) and repeat the global trend analysis for EKE and SST gradients. The global
125 area-integrated extra-tropical EKE and SST gradient trends increase, while the corresponding rel-
126 ative uncertainty decreases; namely, EKE trends are $1.8\% \pm 0.25\%$ per decade and mesoscale SST
127 gradients trends are $1.6\% \pm 0.09\%$ per decade (see striped bars in Fig. 4c,e); both significant at the
128 95% confidence level. It is thus clear that mesoscale activity in the Pacific, and particularly in the
129 equatorial region, is strongly influenced by interannual variability.

130 **Eddy-rich regions become richer**

131 The observed changes in EKE and SST of whole ocean basins integrate over large heteroge-
132 neous regions with opposing trends. For example, the Pacific Ocean aggregates the strengthening
133 of the equatorial currents in the equatorial Pacific Ocean during El Niño events, boundary currents,
134 and the broader-scale oceanic gyres. These dynamical regions are not unique to the Pacific Ocean;
135 the Atlantic and Indian basins also span diverse dynamical regions. Therefore, we further decom-
136 pose the ocean into dynamical regions (Fig. 5d): namely, (1) the Antarctic Circumpolar Current
137 (ACC) and surrounds, (2) the boundary currents and their extensions, (3) the equatorial regions,
138 and (4) the subtropical ocean gyres (see Methods for dynamical region definitions). The remaining
139 regions are aggregated into a fifth group. We then investigate the variability and trends within each
140 of these dynamical sub-regions.

141 Globally, there is a significant increase of EKE and SST gradients, however, each dynam-
142 ical region shows a different response (Fig. 5). For example, the ACC region shows a signif-

143 icant increase in both EKE and SST gradients at rates of 5.1% and 3% per decade (Fig. 5c,e),
144 consistent with an increase in eddy activity with strengthening wind stress, as demonstrated in
145 previous studies^{?, ?, ?}. Boundary currents and their extensions collectively show a similar net re-
146 sponse, in which EKE and SST gradients both increase at rates of 2.5% and 8.1% per decade
147 respectively. Individually, SST gradients increase in all boundary currents, however EKE in the
148 Agulhas retroflection, the East Australian Current, the Leeuwin Current, and the Malvinas Cur-
149 rent have significantly increased, but the Gulf Stream and the Kuroshio Current do not show a
150 significant net strengthening^{?, ?}(Extended Data Fig. 6); instead, regions of increase and decrease
151 tend to cancel each other out in an area-integral. This cancellation is particularly evident for the
152 Kuroshio Current (Fig. 1f and Extended Data Fig. 6b). The response seen in the Gulf Stream and
153 Kuroshio Current is consistent a poleward shift in these currents^{?, ?, ?} and a readjustment to climate
154 modes[?]. Note that a poleward shift cannot be captured by our static climatological definition of
155 the boundary currents regions (see Methods). Thus, a shift of the boundary currents will result in
156 an increase of EKE and SST gradients outside our dynamical definitions (i.e. in regions poleward
157 of the boundary currents and ocean gyres; white regions in Fig. 5d). The observed strengthening
158 of these remaining regions is comparable to that of the ACC, and suggests a poleward shift of the
159 boundary currents, particularly in the Northern Hemisphere.

160 The equatorial and subtropical gyre regions exhibit statistically significant negative SST gra-
161 dient trends, and statistically non-significant negative EKE trends (Fig. 5), suggesting a reduction
162 of the mesoscale eddy variability of the equatorial region and the interior of the subtropical gyres
163 (Fig. 2). The equatorial region is dominated by interannual variability, where large changes corre-

¹⁶⁴ sponding to El Niño events occur in both the EKE and SST gradient time series. The significant
¹⁶⁵ decrease of SST gradients in the subtropical gyres could result from the displacement of the extra-
¹⁶⁶ tropical atmospheric circulation^{?,?} and the expansion of the tropics[?]. The decreasing SST gradient
¹⁶⁷ trends in the tropics could be due to a homogenization of the tropical surface SST gradients. In
¹⁶⁸ the future, the SST gradients induced by mesoscale stirring are expected to reduce as the surface
¹⁶⁹ ocean becomes more thermally homogeneous. However, a longer record is required to separate the
¹⁷⁰ mesoscale response from interannual-decadal climate variability.

¹⁷¹ We have analyzed the available satellite altimetry record of SSH and SST to reveal a signifi-
¹⁷² cant global intensification of the mesoscale eddy field over the satellite record. While the observed
¹⁷³ global surface percentage increases per decade may seem small ($\sim 0.5\%$ per decade), like ocean
¹⁷⁴ heat content and sea-level trends, even small fractions of a percentage change correspond to a large
¹⁷⁵ energy perturbation of the earth system. For example, if we assume that the mesoscale flow ex-
¹⁷⁶ tends vertically to around 500 m depth (a reasonable assumption given the vertical structure of the
¹⁷⁷ gravest mode[?]), then the observed EKE trends integrated over 500 m imply a significant increase
¹⁷⁸ of 0.7% in the global volume-integrated mesoscale energy budget ($13 \times 10^{18} \text{ J}^?$) over the satellite
¹⁷⁹ altimetry record after removing the El Niño signal (Extended Data Fig. 5b). This percentage is
¹⁸⁰ equivalent to $0.9 \times 10^{17} \text{ J}$, the same order of magnitude as the global internal tide energy budget
¹⁸¹ ($1 \times 10^{17} \text{ J}^?$). Eddy kinetic energy in eddy-rich regions, such as boundary current extensions and
¹⁸² the ACC, exhibit even larger significant strengthening of 2% and 5%, respectively (see Fig. 5).
¹⁸³ Increased mesoscale activity observed in both SST and mesoscale SST gradients is most apparent
¹⁸⁴ in regions where eddies are already strong. These eddy-rich regions are critical for carbon and heat

185 uptake by the ocean^{?,?}, and they are known to be sensitive to climate modes that are readjusting
186 in a changing climate; for example, the strengthening of the westerly winds[?] linked to recent in-
187 creasing trends in the Southern Annular Mode^{?,?}. With ongoing future projected changes in the
188 westerly wind belt, it is expected that mesoscale activity in the southern hemisphere boundary cur-
189 rents and the ACC will continue to increase over the coming decades. Current generation models
190 used for climate projections (CMIP6) do not generally resolve mesoscale eddies[?]; thus, important
191 climatic adjustments driven by changes in the eddy field are likely to be missing from these climate
192 projections.

193 The mesoscale evolution described here cannot be captured by coarse-resolution reanalysis
194 products and sparse Argo float observations, as previously used in other studies[?]. Here we have
195 used eddy-permitting satellite observations to reveal a potential decrease in EKE over the tropics,
196 while reanalysis products suggest the tropics is where KE anomalies have increased the most[?].
197 The KE anomaly differs from EKE because it contains the time-mean flow in addition to the time-
198 varying components. The source of differences between Hu *et al.*, (2020)[?] and our results can be
199 assessed by an analysis of the ocean KE anomaly using satellite observations. The KE anomaly
200 trends are almost identical to the EKE trends presented above (compare Fig. 1 and Extended Data
201 Fig. 7), yet strikingly different from those obtained by Hu *et al.*, (2020) (their Fig 2a). This sug-
202 gests that the difference between our results and those of Hu *et al.*, (2020) arises from the inability
203 of reanalyses and the Argo dataset to resolve the mesoscale, due to coarse-resolution and sparse
204 sampling, rather than from the definition of the KE anomaly. An alternative explanation of the
205 differences between our study and Hu *et al.*, (2020) could arise from the KE anomaly trends in Hu

206 *et al.*, (2020) being depth-integrated (0-2000 m), while our EKE calculations are derived solely
207 from surface diagnostics. In addition, as we have demonstrated, the tropics are strongly influenced
208 by interannual variability (e.g. El Niño), and yet the KE time-series from coarse reanalysis data
209 does not detect the two extreme El Niño events observed in the satellite record. Thus, data res-
210 olution and/or subsurface ocean dynamics are the likely causes of the discrepancy between our
211 eddy-permitting analysis and the results from prior work using reanalysis products?.

212 There are several possible causes of the observed trends in mesoscale activity including (1)
213 changes in winds (wind curl, wind stress), (2) changes in stratification, and (3) changes in large-
214 scale horizontal temperature gradients. These forcing agents can impact the eddy activity via
215 a combination of processes, e.g., non-local intensification of winds, outcropping and tilting of
216 isopycnals, and strengthening of baroclinic instability. Atmospheric reanalyses show distinct and
217 inconsistent wind stress trend patterns, while records of *in situ* measurements of isopycnal tilt and
218 baroclinic growth rate are too short and too sparse to provide evidence of a dynamical mechanism
219 driving the observed increase in eddy activity. Thus, longer observational records with higher tem-
220 poral and spatial frequency are required to better understand the increase in EKE observed from
221 satellites. In addition, as discussed above, trends computed from coarse-resolution ocean reanal-
222 ysis products? with parameterized mesoscale eddies differ significantly from the mesoscale trends
223 we detect from eddy-resolving satellite altimetry. Hence, an in-depth analysis of the dynamics
224 leading to the observed mesoscale eddy evolution should be explored in more detail using truly
225 eddy-resolving global ocean models or eddy-resolving reanalysis products.

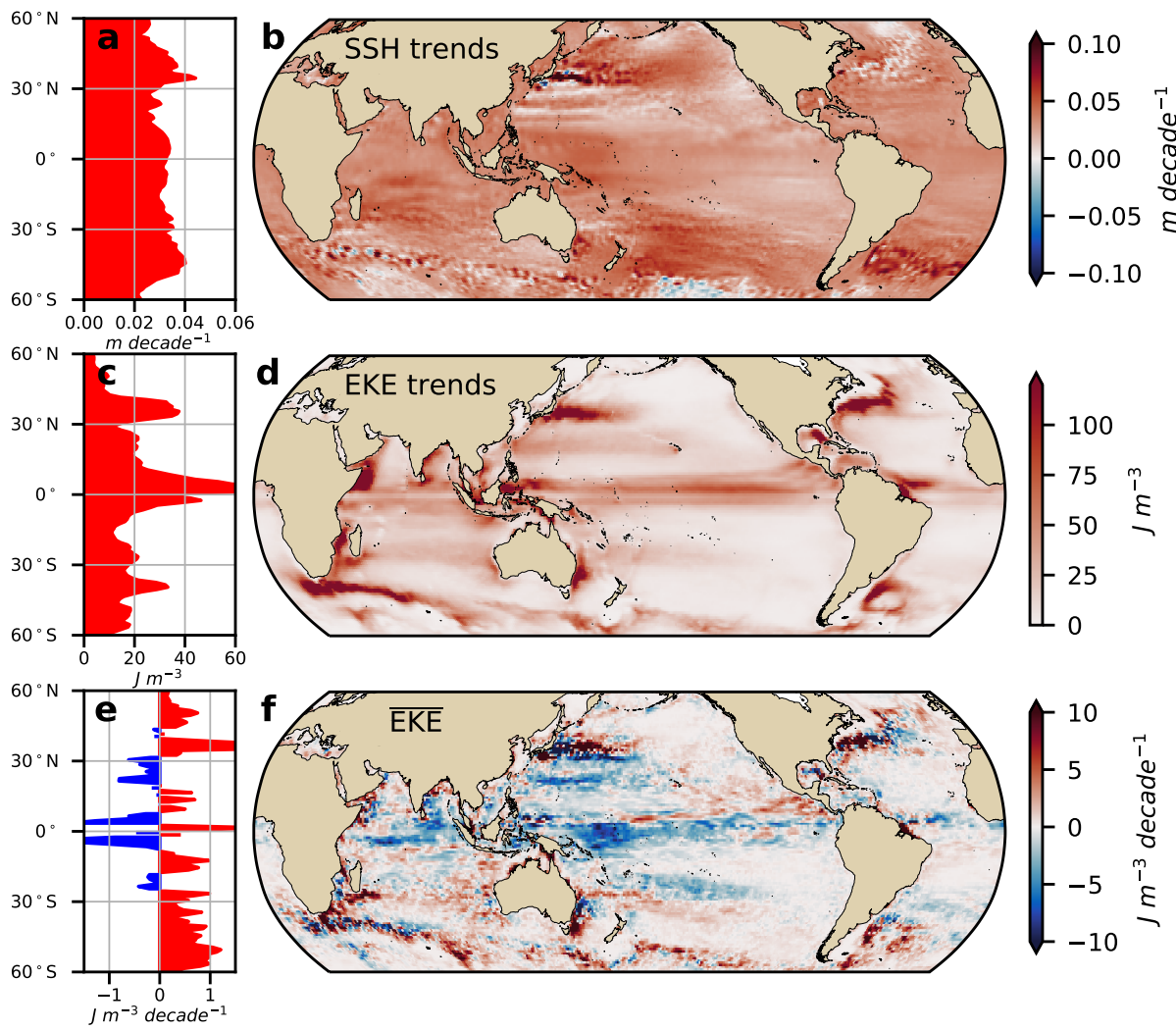
226 Our study has documented a major global-scale reorganization of the ocean's mesoscale
227 kinetic energy observed over the past three decades. These observed adjustments in the mesoscale
228 field have the potential to affect ocean circulation at regional and global scales, and to modify
229 the transport and redistribution of tracers, such as heat, carbon, and nutrients. Our findings thus
230 have major implications for ocean readjustment to a changing climate, as the enhancement of the
231 mesoscale ocean currents may feed back on the sequestration of anthropogenic heat and carbon
232 into the ocean.

233 **Acknowledgments**

234 We thank Ryan Holmes for clarifying the equatorial response of El Niño events during 1997-
235 1998 and 2015-2016. We thank the reviewers for their insightful comments and suggestions. The
236 satellite altimetry products were produced by Ssalto/Duacs and distributed by AVISO+, with sup-
237 port from CNES (<https://www.aviso.altimetry.fr/en/data/products/sea-surface-heig>
238 global/gridded-sea-level-heights-and-derived-variables.html). J. M.-
239 M. was supported by the Consejo Nacional de Ciencia y Tecnología (CONACYT), Mexico fund-
240 ing. M.H.E. was supported by the Centre for Southern Hemisphere Oceans Research (CSHOR),
241 a joint research centre between QNLM, CSIRO, UNSW and UTAS. A. K. M. was supported by
242 the Australian Research Council DECRA Fellowship DE170100184. Analyses were undertaken
243 on the National Computational Infrastructure in Canberra, Australia, which is supported by the
244 Australian Commonwealth Government.

245 **Author contributions**

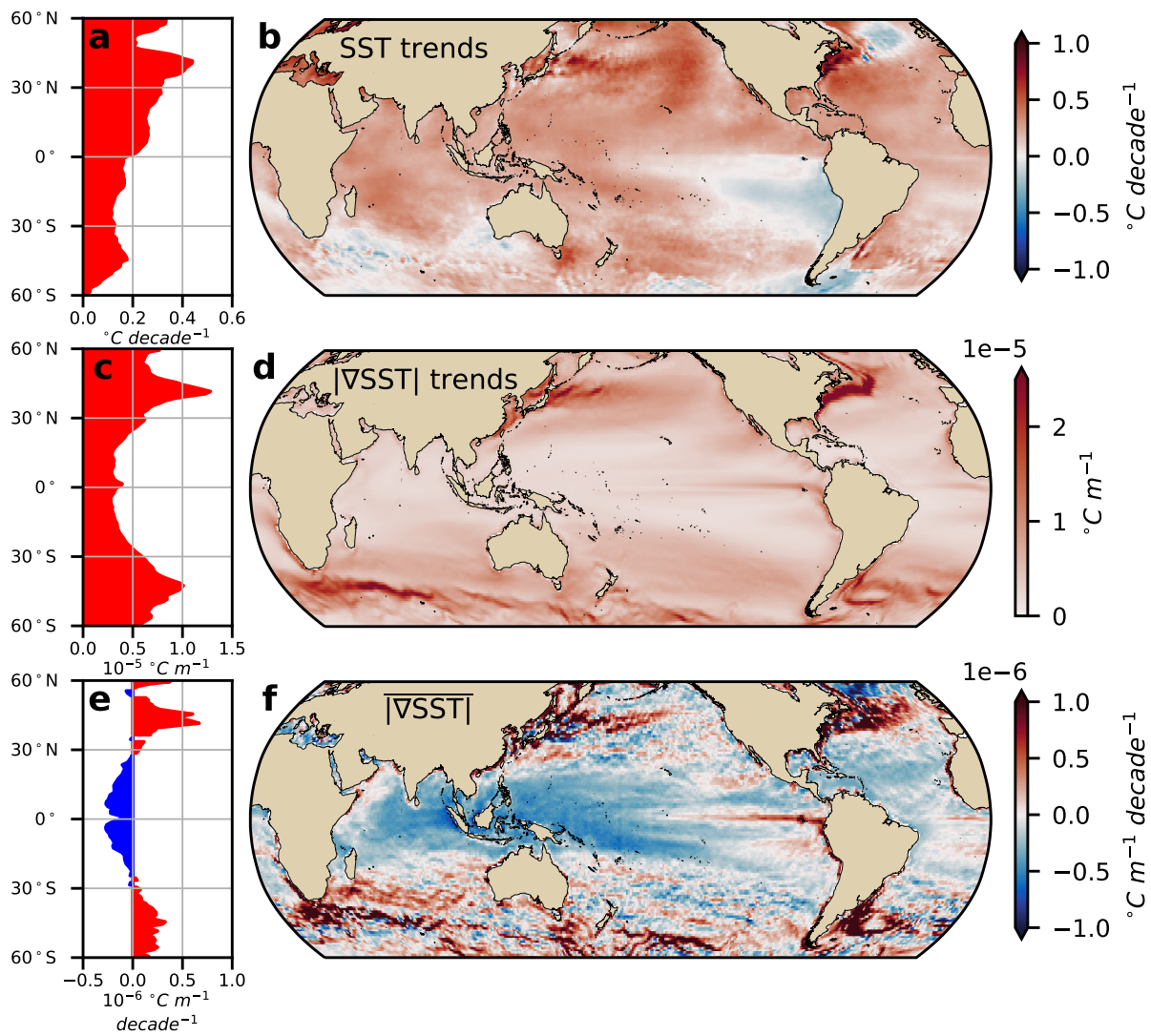
²⁴⁶ J.M.M, A.McC.H. and M.H.E. conceived the study. J.M.M. conducted the analyses. All
²⁴⁷ authors contributed to interpretation, writing and revision of the manuscript.



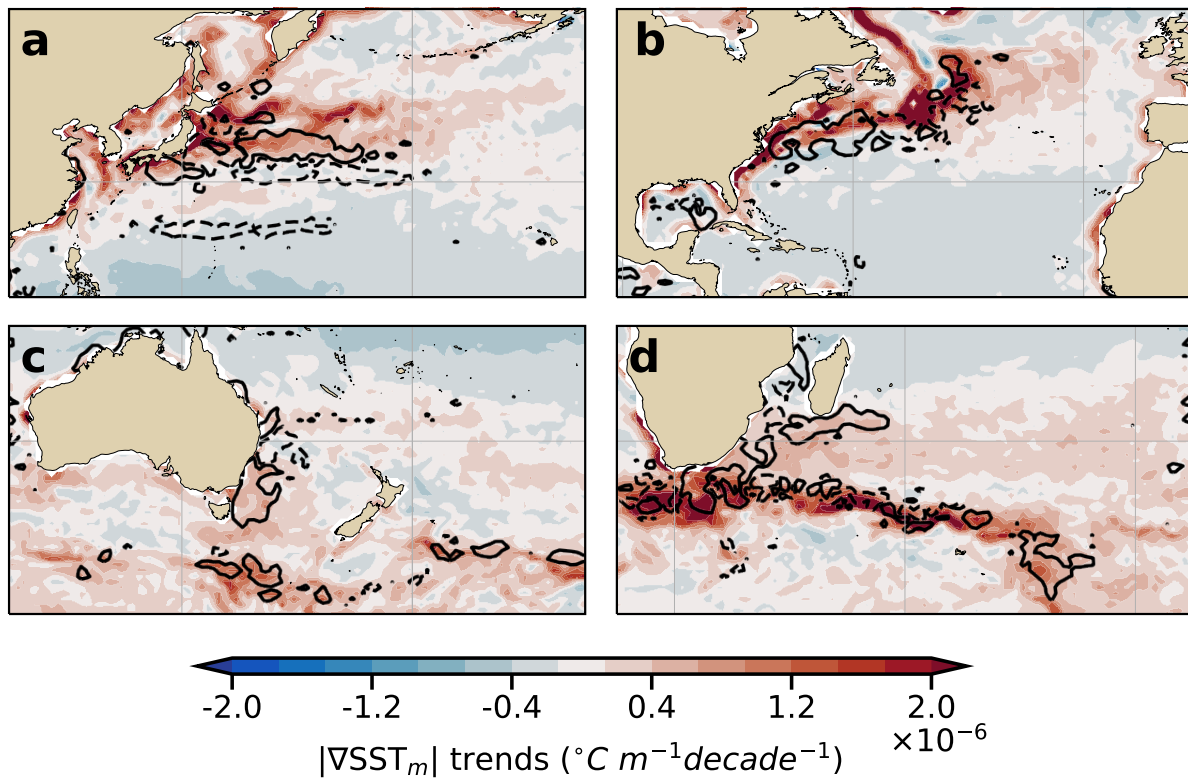
248

249

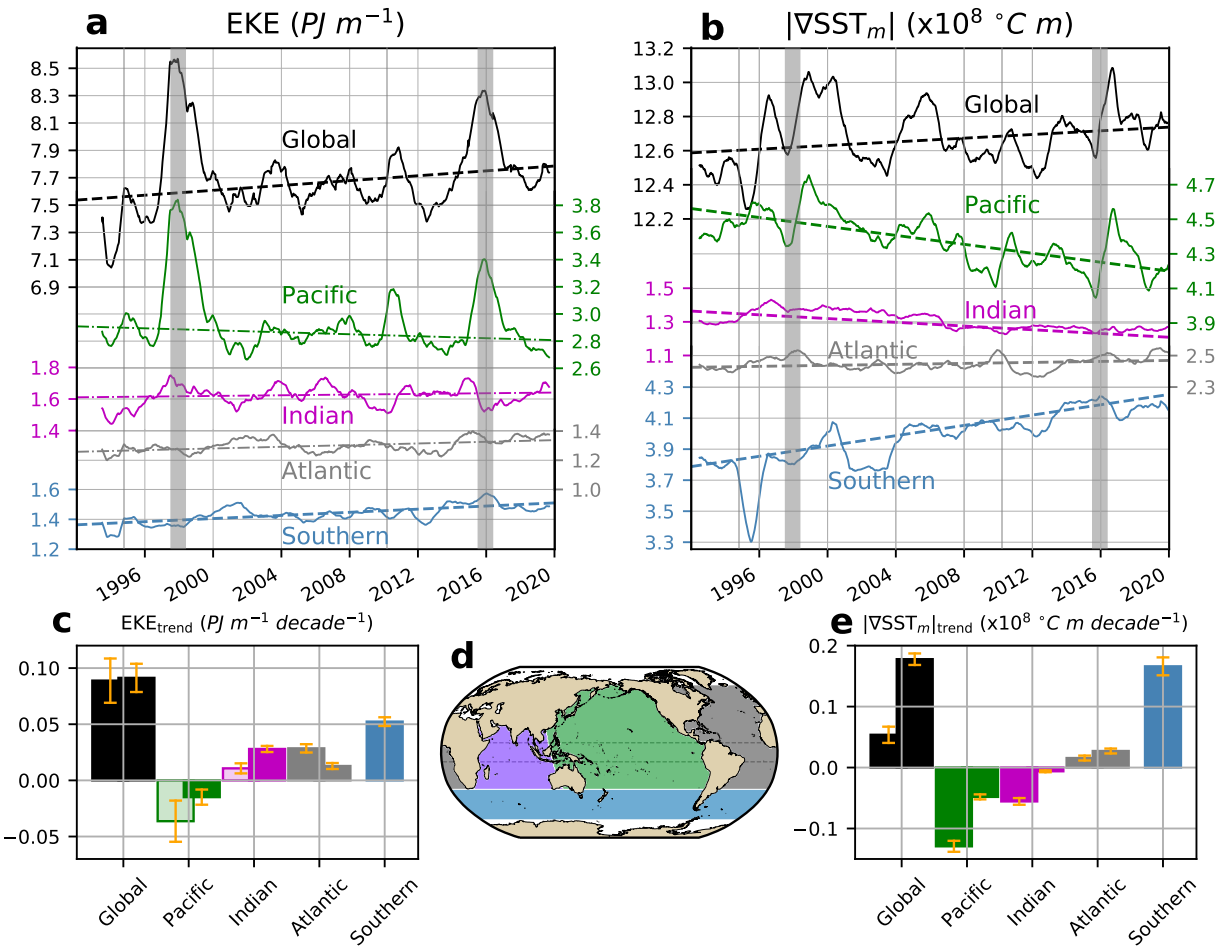
Figure 1 Sea surface height (SSH) trend, mean surface eddy kinetic energy (EKE) and surface eddy kinetic energy trend between 1993-2020 (a) Zonally averaged SSH trend; (b) map of SSH trend (92.1% of area is statistically significant above the 95% confidence level; for spatial distribution refer to Extended Data Fig. 1a); (c) zonally averaged mean EKE; (d) map of mean EKE; (e) zonally averaged EKE trend; (f) map of EKE trend (55.4% of area is statistically significant above the 95% confidence level; see Extended Data Fig. 1b).



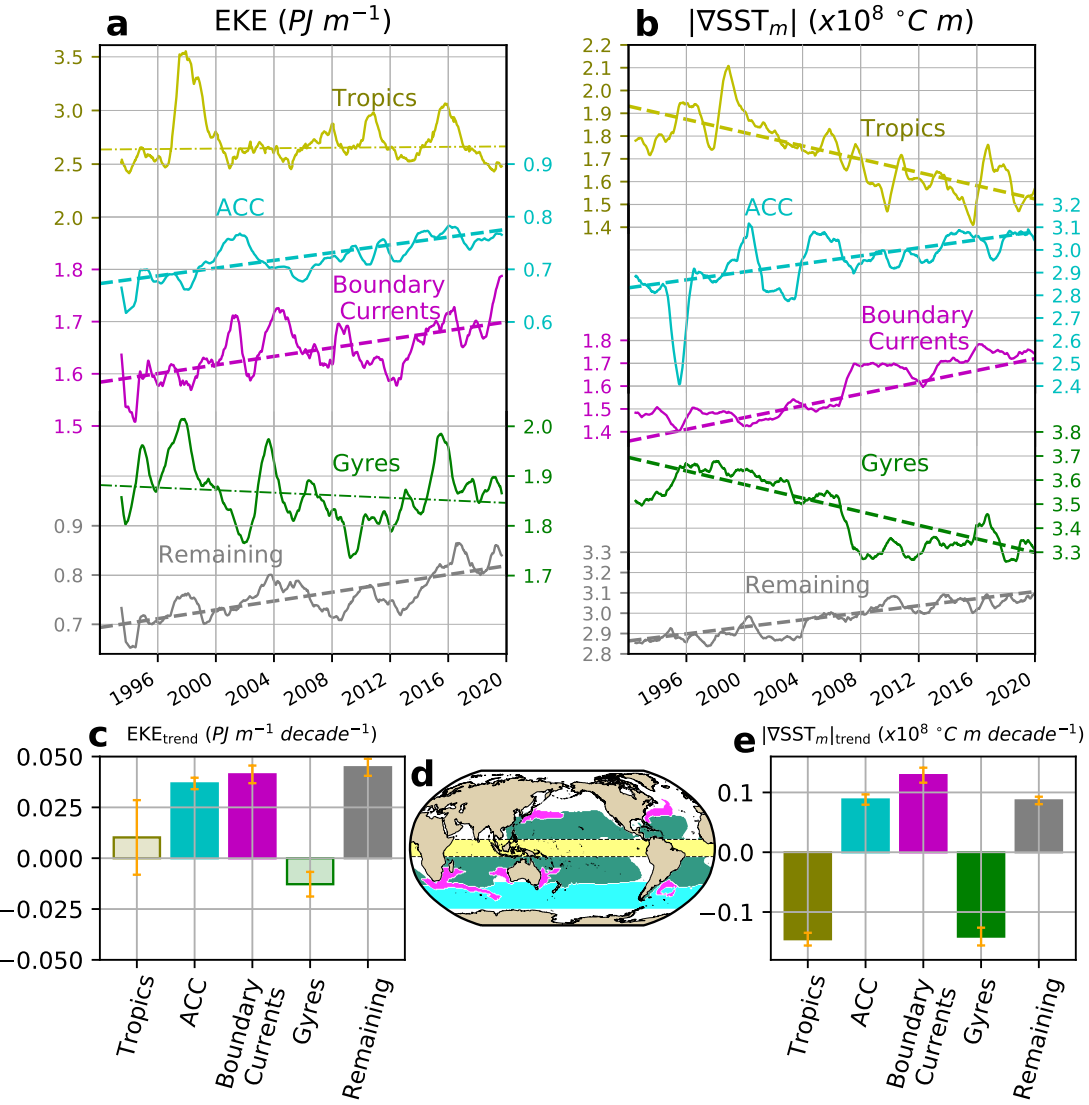
256
257 **Figure 2 Sea surface temperature (SST) trends, mean SST gradient magnitude, and**
258 **SST gradient magnitude trends between 1993-2020.** (a) Zonally averaged SST trend;
259 (b) map of SST trend (76.7% of area is statistically significant above the 95% confidence
260 level; for the spatial distribution refer to Extended Data Fig. 1c); (c) zonally averaged
261 time-mean of SST gradient magnitude; (d) map of time-mean of SST gradient magnitude;
262 (e) zonally averaged SST gradient magnitude trend; (f) map of SST gradient magnitude
263 trends (81.6% of area is statistically significant above the 95% confidence level; see Ex-
264 tended Data Fig. 1d). Note that the spatial pattern of SST gradient maps is independent
265 of the temporal extent of the SST gradient record used to compute SST gradient trends
266 (Extended Data Fig. 2).



267
268 **Figure 3 Regional maps of mesoscale SST gradient magnitude trends and surface**
269 **EKE trends.** (a) Kuroshio Current; (b) Gulf Stream; (c) East Australian Current; (d) Ag-
270 ulhas retroreflection. In all panels, mesoscale SST gradient magnitude trends are shown
271 by the background color, solid contours show positive EKE trends and dashed contours
272 show negative EKE trends (contours of $\pm 5 \text{ J } m^{-3} \text{ decade}^{-1}$).



273
274 **Figure 4 Time-series and linear trends of area integrated surface EKE and mesoscale**
275 **SST gradient magnitudes over various ocean basins.** Global (solid black), Southern
276 (blue), Indian (magenta), Pacific (green), and Atlantic Oceans (gray) and each region
277 separately without the equatorial region (striped bars). (a) Surface EKE time series. (b)
278 mesoscale SST gradient magnitude time series. In panels (a) and (b), solid curves de-
279 note 12-month running averages for each basin, dashed lines correspond to statistically
280 significant time-series trends, dashed-dotted lines show statistically insignificant time-
281 series trends, and vertical gray bars indicate El Niño events (above the 90th percentile
282 of MEI.v2²). Note that the y axis is discontinuous in panels (a) and (b). (c) Linear EKE
283 trends for each basin. (d) Ocean basins; equatorial region (9°S–9°N) is marked by the
284 dashed lines. (e) Linear mesoscale SST gradient trends. In panels (c) and (e), stan-
285 dard errors are shown with orange bars and statistically significant trends (above the 95%
286 confidence level) are solid bars while non-significant trends are translucent.



287
288 **Figure 5 Time-series and linear trends of integrated surface EKE and mesoscale**
289 **SST gradient magnitudes over dynamical regions.** Global ocean (black), Tropics (yellow),
290 Antarctic Circumpolar Current (cyan), boundary currents and their extensions (magenta),
291 subtropical ocean gyres (green) and the rest (gray). (a) Surface EKE time-series.
292 (b) mesoscale SST gradient magnitude time-series. In panels (a) and (b), solid color
293 curves are 12-month running for each region, dashed lines correspond to statistically sig-
294 nificant time-series trends, and dashed-dotted lines show insignificant time-series trends.
295 (c) Linear EKE trends for each dynamical region. (d) Definition of ocean regions. (e) Lin-
296 ear mesoscale SST gradient trends. Note that in panel (a) the top curve that corresponds
297 to the Tropics has a different scale than the rest. In panels (c) and (e), standard errors
298 are shown with orange bars and statistically significant trends (above the 95% confidence
299 level) are solid bars while non-significant trends are translucent.

300 **Methods**

301 **Observational products**

302 The data used in this study includes sea surface height, geostrophic velocities, and sea sur-
303 face temperature. The Archiving, Validation and Interpretation of Satellite Oceanographic data
304 (AVISO+) gridded multi-mission sea surface height and geostrophic velocities have a horizontal
305 resolution of $1/4^\circ$ (although the effective resolution may be coarser in some regions [?]). Currents
306 within the equatorial region ($5^\circ S$ - $5^\circ N$) are estimated using an equatorial β -plane approximation
307 of the geostrophic equations[?]. National Oceanic and Atmospheric Administration - Optimum In-
308 terpolation Sea Surface Temperature (NOAA-OISST) has a horizontal resolution of $1/4^\circ$ [?]. This
309 dataset is constructed by combining observations from different products (e.g. satellites, ships,
310 buoys, and Argo floats).

311 These datasets have a quasi-global coverage ($65^\circ S$ - $65^\circ N$) and span 27 years, from January
312 1993 to March 2020. The SST product is available for a longer duration, but we only analyze the
313 period of overlap with the AVISO+ record (see Extended Data Fig. 2). Anomalies were computed
314 with respect to the record's climatology. We have verified that using a different period for defining
315 the climatology does not change the observed trends in the anomaly fields. We have also veri-
316 fied through wavelet analysis of the time-series at individual points that there is no evidence that
317 steps in the record occurred due to improved technology in satellite missions and oceanographic
318 observations.

319 **Kinetic energy decomposition**

320 Kinetic energy (KE) density is decomposed into the energy density contained by the steady
 321 flow (time-mean) and that contained by the transient flow (time-varying). In other words, the
 322 surface geostrophic velocity components are split using a Reynolds decomposition into their time-
 323 mean (\bar{u} , \bar{v}) and time-varying components ($u' = u - \bar{u}$, $v' = v - \bar{v}$), with bars denoting time-
 324 averages over the whole record. The terms u' and v' are the anomalies of the surface geostrophic
 325 velocities provided by AVISO+, which are proportional to the AVISO+ SSH gradients (via the
 326 geostrophic approximation and equatorial beta-plane approximation). The KE is, therefore, de-
 327 composed as:

$$328 \underbrace{\frac{1}{2}\rho_0(u^2 + v^2)}_{\text{KE}} = \underbrace{\frac{1}{2}\rho_0(u'^2 + v'^2)}_{\text{EKE}} + \underbrace{\frac{1}{2}\rho_0(\bar{u}^2 + \bar{v}^2)}_{\text{MKE}} + \underbrace{\rho_0(\bar{u}u' + \bar{v}v')}_{\text{Cross terms}}, \quad (1)$$

329 where we approximate the density of the seawater by the constant $\rho_0 = 1025 \text{ kg m}^{-3}$. The
 330 energy contained in the time-varying component of the flow is known as the eddy kinetic energy
 331 (EKE), while the mean kinetic energy (MKE) is the energy of the time-mean flow.

332 Maps of EKE in this study correspond to the the time-mean EKE, defined as

$$333 \overline{\text{EKE}}(x, y) = \overline{\frac{1}{2}\rho_0(u'^2 + v'^2)}, \quad (2)$$

334 where the units of $\overline{\text{EKE}}(x, y)$ are Jm^{-3} . Time-series correspond to the surface area-integrated
 335 EKE (globally or over specific regions).

$$336 \langle \text{EKE} \rangle(t) = \iint_A \frac{1}{2}\rho_0(u'^2 + v'^2) dx dy, \quad (3)$$

337 where A refers to the area of each geographical or dynamical region, angle brackets $\langle \rangle$ denote the
 338 area integral, and $\langle \text{EKE} \rangle(t)$ has units of Jm^{-1} , as it is multiplied by the grid area.

339 Furthermore, the velocity field was decomposed into mesoscale (u_m, v_m ; scales smaller than
 340 3°) and large-scale (u_{ls}, v_{ls} ; scales larger than 3°). To decompose the velocity field, we first
 341 compute large-scale u_{ls} and v_{ls} by a spatial convolution with a constant $3^\circ \times 3^\circ$ kernel K :

$$342 \quad \vec{u}_{ls}(x, y, t) = \frac{\iint \vec{u}(x - x', y - y', t) K(x', y') dx' dy'}{\iint K(x', y') dx' dy'}, \quad (4)$$

343 the mesoscale \vec{u}_m is defined as:

$$344 \quad \vec{u}_m = \vec{u} - \vec{u}_{ls}. \quad (5)$$

345 Then the mesoscale and large-scale EKE can be computed using these velocity fields.

346 Sea surface temperature gradients

347 Analogous to mesoscale and large-scale EKE, sea surface temperature (SST) gradients are
 348 decomposed into mesoscale (SST gradients with scales smaller than 3°) and large-scale (SST gra-
 349 dients with scales larger than 3°). To decompose the SST gradients, we first compute large-scale
 350 SST by using a spatial convolution with a constant $3^\circ \times 3^\circ$ kernel K , and a 12-month running
 351 average i.e.,

$$352 \quad \text{SST}_{ls}(x, y, t) = \frac{\iint \widetilde{\text{SST}}(x - x', y - y', t) K(x', y') dx' dy'}{\iint K(x', y') dx' dy'}, \quad (6)$$

353 where the tilde $\widetilde{}$ denotes a 12-month running average. The mesoscale SST is then defined as

$$354 \quad \text{SST}_m = \text{SST} - \text{SST}_{ls}. \quad (7)$$

355 The gradients of the large-scale and mesoscale SST are computed afterwards. The SST

356 gradient magnitude is:

$$357 \quad |\nabla \text{SST}| = \sqrt{\left(\frac{\partial \text{SST}}{\partial x}\right)^2 + \left(\frac{\partial \text{SST}}{\partial y}\right)^2}, \quad (8)$$

358 with analogous expressions for SST_m and SST_{ls} .

359 Computations of SST gradient time-series and time mean SST gradient trend maps are anal-

360 ogous to those of EKE, e.g. the area-integrated SST gradients:

$$361 \quad \langle|\nabla \text{SST}|\rangle(t) = \iint_A |\nabla \text{SST}| \, dx \, dy, \quad (9)$$

362 Trends, significance & uncertainties

363 Linear trends are calculated using a linear least-squares regression for spatially integrated
364 time-series. For trend maps the fields are first coarsened to a $1^\circ \times 1^\circ$ grid, and then the linear trends
365 are computed for each grid point. All the observed trends for EKE and SST gradients (time-series
366 and trend maps) are assessed using a Theil-Sen estimator, while the statistical significance uses a
367 modified Mann-Kendall test⁷. This statistical test takes into account autocorrelations within the
368 time-series. Finally, the reported uncertainties in figures 4c,e and 5c,e correspond to the standard
369 error using the effective sample size from the Mann–Kendall test; that is, the standard deviation of
370 the time-series divided by the square root of the effective sample size.

371 Geographical and dynamical regions

372 Geographical regions consist of the following ocean basins (see Fig.4d): the Southern Ocean
373 (south of 35°S), the Indian Ocean, the Pacific Ocean and the Atlantic Ocean. These ocean basins
374 were defined to capture ocean processes at all scales. The ocean basin mask can be obtained

375 from the repository https://github.com/josuemtzmo/EKE_SST_trends that contains
376 all the data used for this study (refer to acknowledgments; filename `ocean_basin_mask.nc`).

377 Dynamical regions were defined from the climatological mean SSH and the mean KE (see
378 Fig.5d). We defined a mask for each dynamical region, then we extracted and masked each dy-
379 namical region in the following order, to avoid any overlap between regions:

- 380 1. the equatorial region is defined as the region between 9°S and 9°N,
- 381 2. the boundary currents and their extensions are defined as regions with mean KE above the
382 ~99-th percentile (2.8σ). Note that the Peruvian and Californian currents are weaker (below
383 the 99th percentile of mean KE) and, therefore, according to our definition, they do not
384 qualify as boundary currents.
- 385 3. the subtropical gyre masks depend on each ocean basin: the Pacific Ocean gyres correspond
386 to mean SSH above the 0.65 m contour; the Atlantic Ocean gyres correspond to mean SSH
387 above the 0.36 m contour; and the Indian Ocean gyres correspond to mean SSH above the
388 0.60 m contour. All these values were tuned to approximately capture the same extension as
389 the theoretical estimation of ocean gyres according to the Sverdrup balance, and
- 390 4. the Antarctic Circumpolar Current and its surrounding areas (ACC) is defined as all remain-
391 ing regions left between 35°S - 60°S.

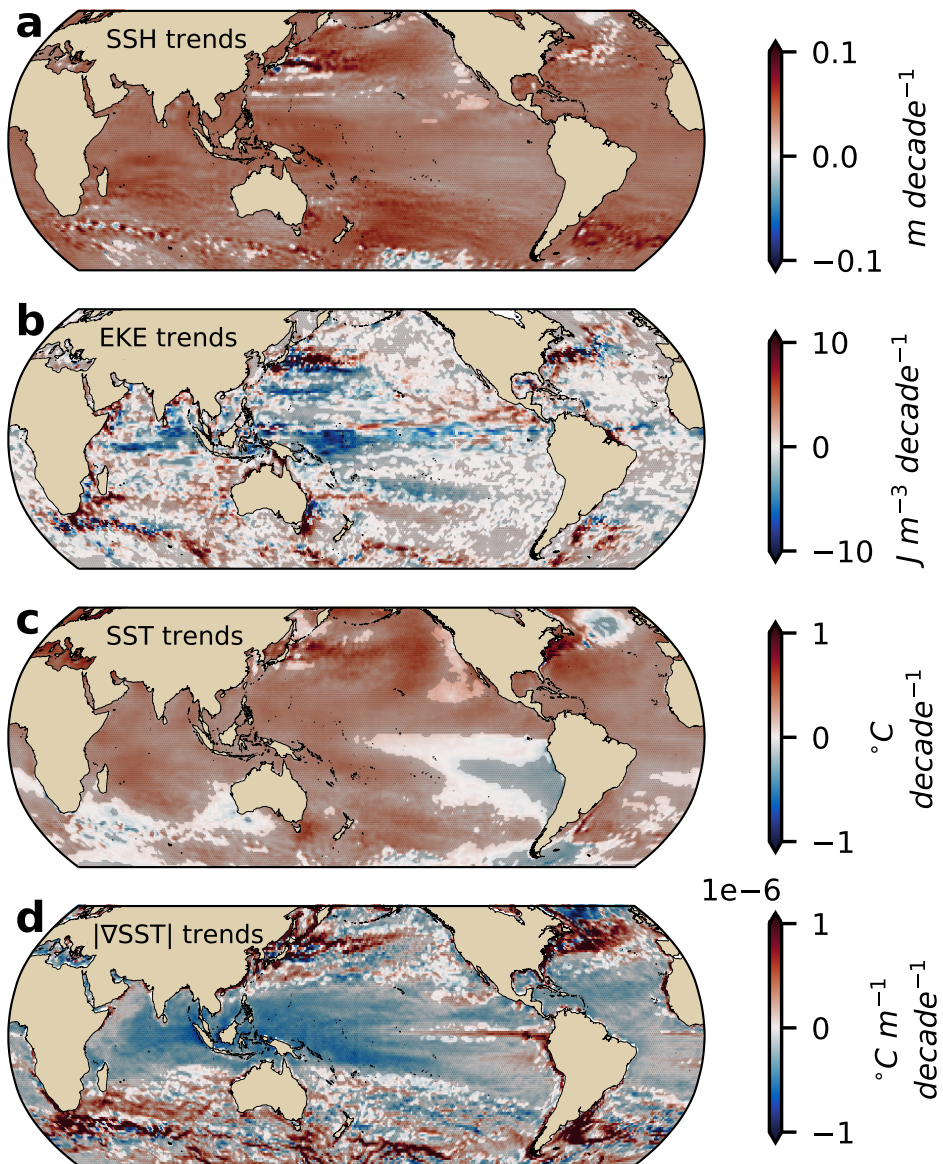
392 The dynamical regional mask can be obtained from the repository containing all the data used for
393 this study (refer to acknowledgments; filename `ocean_processes_mask.nc`).

394 **Data availability**

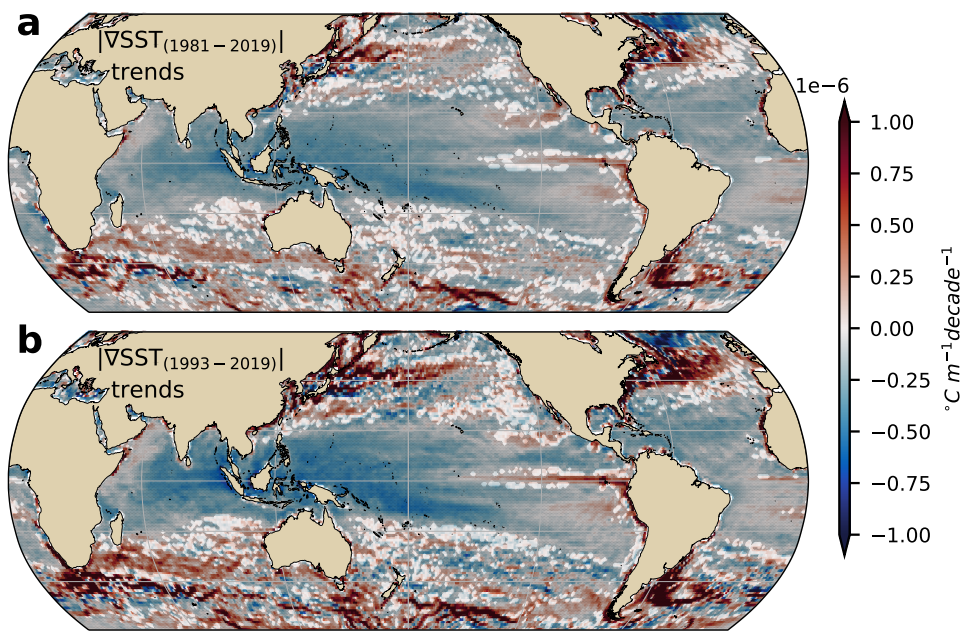
395 The unprocessed data from the satellite altimetry (produced by Ssalto/Duacs and distributed
396 by AVISO+) can be found at: <https://www.aviso.altimetry.fr/en/data/products/>
397 sea-surface-height-products/global/gridded-sea-level-heights-and-derived-væ
398 html). The processed data used in this study is publicly available in netCDF format at <https://doi.org/10.5281/zenodo.3993824>.
399

400 **Code availability**

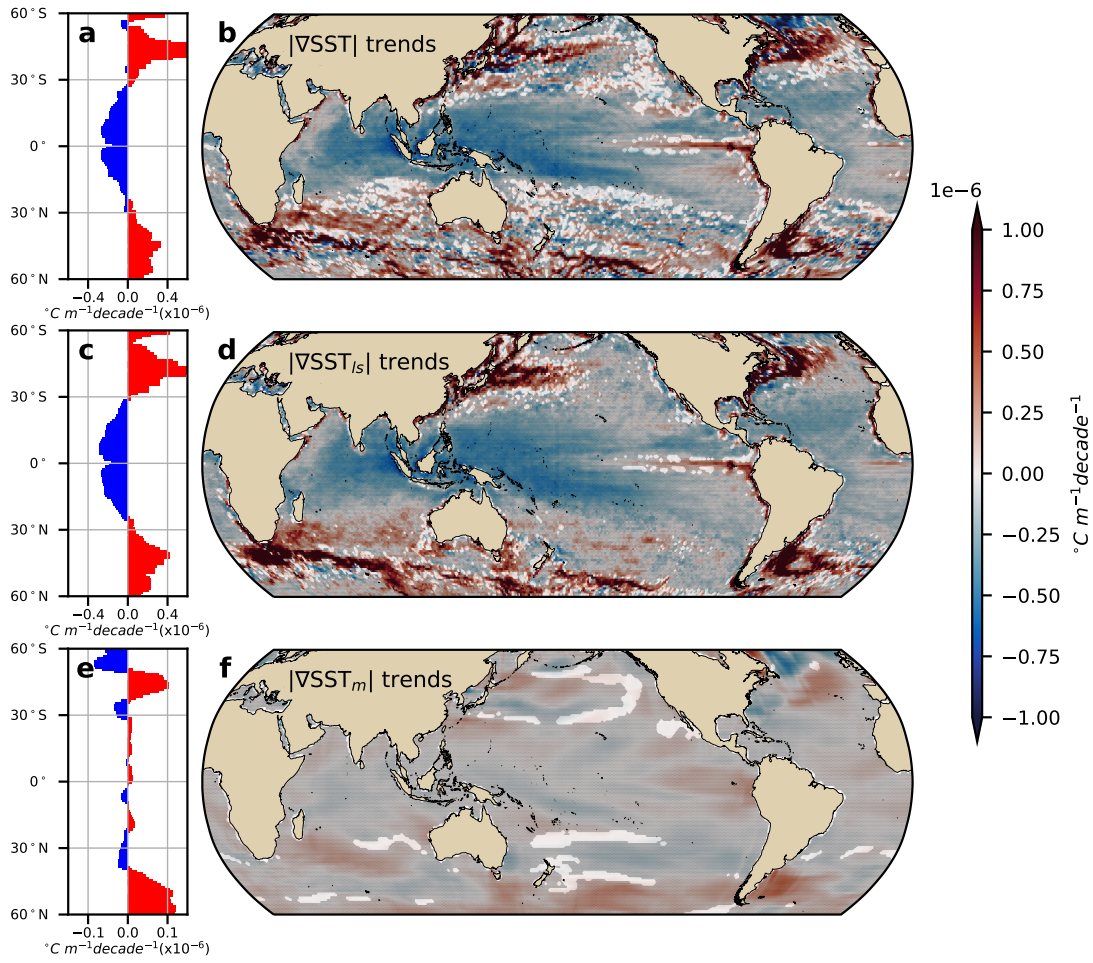
401 All plots were generated using Python 3.8. Additional information and notebooks that repro-
402 duce the figures and analysis can be found at [https://github.com/josuemtzmo/EKE_](https://github.com/josuemtzmo/EKE_SST_trends)
403 SST_trends.

404 **Extended data**

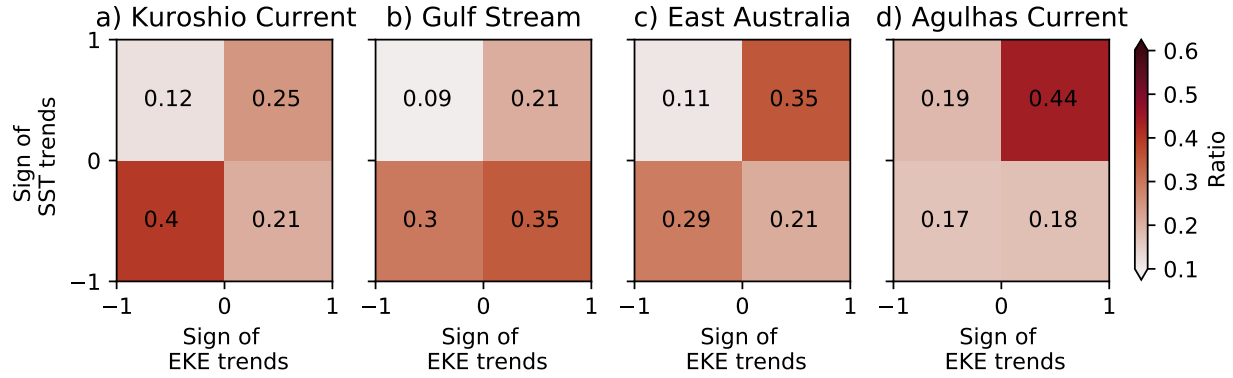
405
406 **Extended Data Figure 1 | Regions of statistically significant trends of (a) sea sur-**
407 **face height; (b) surface eddy kinetic energy; (c) sea surface temperature; (d) sea**
408 **surface temperature gradient magnitude.** As per Figs. 1b, 1f, 2b, and 2f in main
409 manuscript, but showing in gray stippling regions that are statistically significant above
410 the 95% confidence level.



411
 412 **Extended Data Figure 2 | Sea surface temperature gradient magnitude trends for**
 413 **periods between 1981-2020 and 1993-2020.** Gray stippling shows regions that are sta-
 414 tistically significant above the 95% confidence level.



415
 416 **Extended Data Figure 3 | Sea surface temperature gradient magnitude trend scale**
 417 **analysis.** Large-scale SST gradient magnitudes are computed by filtering the SST field
 418 with a 3° kernel filter and a running average of 12 months before computing the gradient
 419 magnitudes and their respective trends (see Methods). The small scales correspond to
 420 the gradients of the SST minus the large-scale filtered SST field. (a) Zonally averaged
 421 SST gradient magnitude trends; (b) map of SST gradient magnitude trends; (c) zonally
 422 averaged small-scale SST gradient magnitude trends; (d) map of small-scale SST gradi-
 423 ent magnitude trends; (e) zonally averaged large-scale SST gradient magnitude trends; (f)
 424 map of large-scale SST gradient magnitude trends. In panels (b), (d) and (f) gray stippling
 425 shows regions where the trends are statistically significant above the 95% confidence
 426 level.

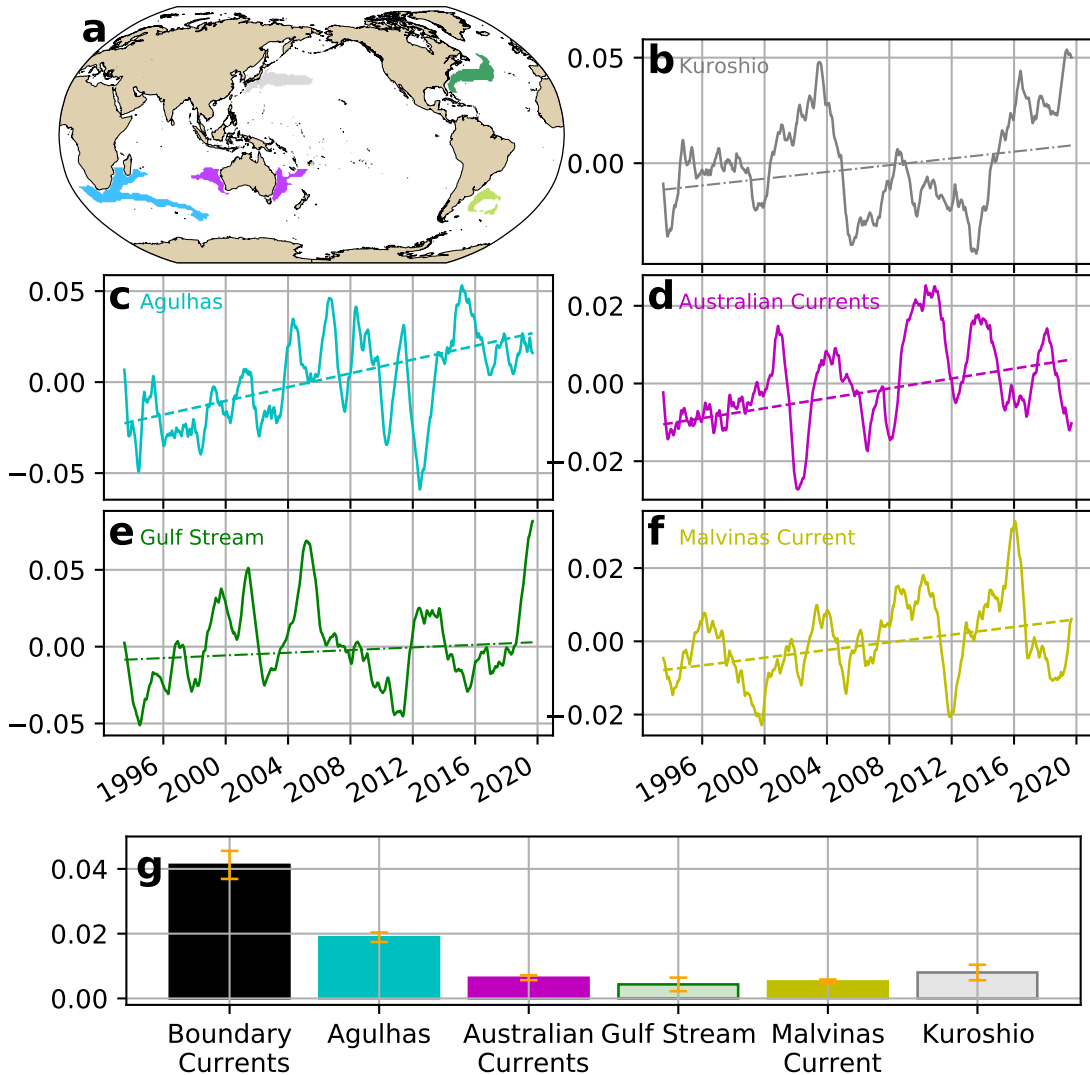


427
 428
 429 **Extended Data Figure 4 | Regional ratio of mesoscale SST gradient magnitude**
 430 **trends and surface EKE trends signs.** (a) Kuroshio current; (b) Gulf Stream; (c) East
 431 Australian Current; (d) Agulhas retroflection. The ratio was computed by integrating the
 432 area weighted sign of the SST gradient magnitude trends and surface EKE trends divided
 433 by the total area of the region plotted in the Fig. 3. Quadrants I and III of each panel
 434 show colocated regions with the same sign in SST gradients and EKE trends, more than
 435 60% of the signs in the (a) Kuroshio current, (c) East Australian Current, and (d) Agulhas
 436 retroflection are colocated.

437

438 **Extended Data Figure 5 | Surface eddy kinetic energy time-series and trends com-**
439 **puted from filtered velocities.** Scales larger than typical mesoscale are computed by
440 filtering the surface velocity fields with a 3° kernel filter (u_{ls}), and the smaller scales are cal-
441 culated from the difference of the velocity fields and the filtered velocity field ($u_e = u - u_{ls}$).
442 Then surface EKE and their respective trends are computed (see Methods). (a) EKE time
443 series of scales larger than 3 degrees time series; (b) EKE time series of scales smaller
444 than 3 degrees; (c) map of large-scale EKE trends; (d) map of small-scale EKE trends.
445 Text in panels (a) and (b) correspond to trends per decade.

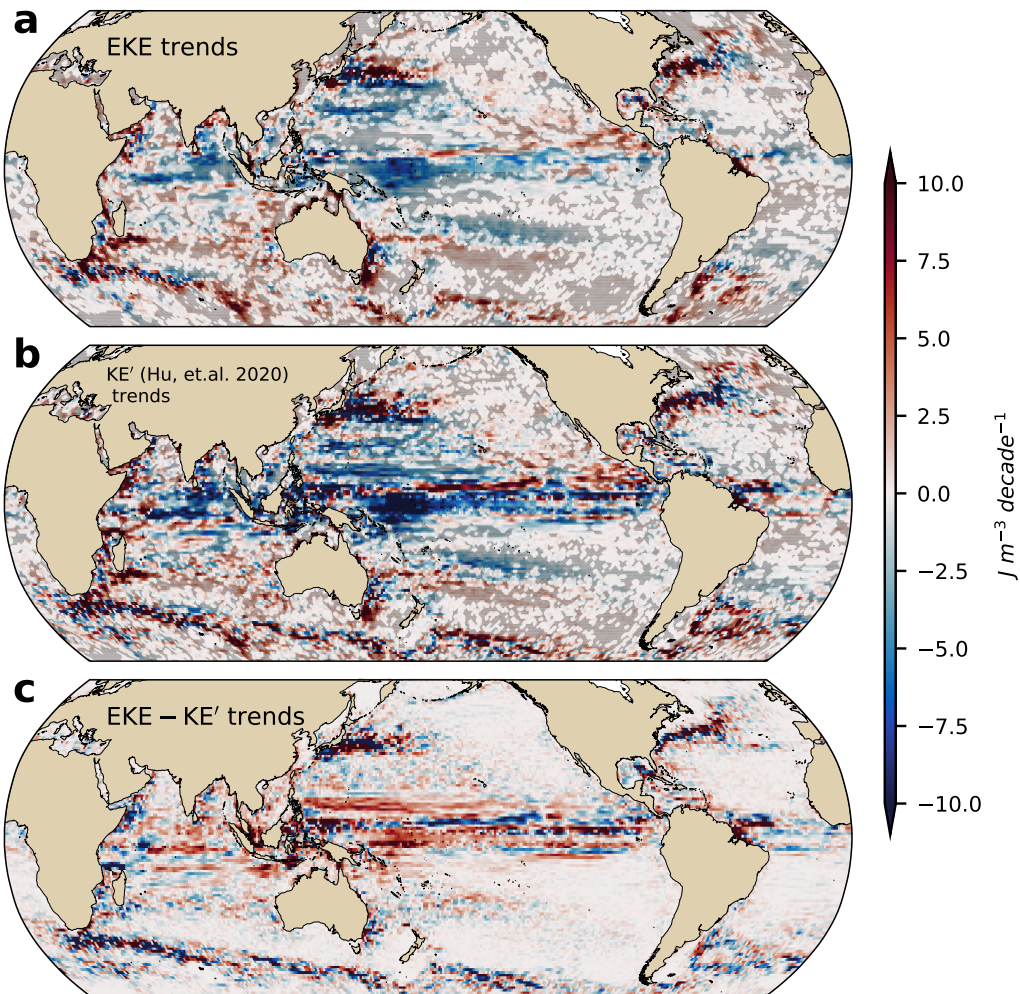
./figures/large_scale_vs_small_scalle_eke.pdf



446

447

Extended Data Figure 6 | Time-series and trends of surface eddy kinetic energy integrated over boundary currents. (a) Map of boundary current regions defined from climatological mean EKE and time series anomalies ($PJ\ m^{-1}$) and trends ($PJ\ m^{-1}\ decade^{-1}$) for each boundary current : (b) Kuroshio Current; (c) Agulhas Current; (d) East Australian Current and Leeuwin Current; (e) Gulf Stream; (f) Malvinas Current. (g) Linear EKE trends for boundary currents, uncertainties are shown in orange bars and statistically significant trends (above the 95% confidence level) are denoted with solid bars while non-significant trends are translucent.



455
 456 **Extended Data Figure 7 | Comparison of satellite trends using surface EKE and**
 457 **kinetic energy anomaly (KE') as computed by Hu et al., 2020** ? (a) EKE trend map, (b)
 458 KE' trend map, and (c) difference between EKE and KE' trends. The difference between
 459 the fields is a consequence of the cross terms due to the Reynolds velocity decomposi-
 460 tion. In panel (a) and (b) gray stippling shows regions where the trends are statistically
 461 significant above the 95% confidence level.